

Determination of the 3D shape of a nanoscale crystal with atomic resolution from a single image

C. L. Jia^{1,2,3*}, S. B. Mi¹, J. Barthel^{3,4}, D. W. Wang¹, R. E. Dunin-Borkowski^{2,3},
K. W. Urban^{2,3} and A. Thust^{2,3}

¹International Center for Dielectric Research, Xi'an Jiaotong University, Xi'an, China

²Peter Grünberg Institute, Forschungszentrum Jülich GmbH, Jülich, Germany

³Ernst Ruska-Centre for Microscopy and Spectroscopy with Electrons,
Forschungszentrum Jülich GmbH, Jülich, Germany

⁴Central Facility for Electron Microscopy, RWTH Aachen University, Aachen, Germany

*e-mail: c.jia@mail.xjtu.edu.cn; c.jia@fz-juelich.de

Evaluation of the absolute image intensity

Quantitative high-resolution transmission electron microscopy has been affected by a long-standing problem, which is known as the factor-of-three problem, or the Stobbs factor problem¹. This problem reflects a commonly observed discrepancy between the image contrast found in experiment and simulation, whereby the contrast in image simulations is found to be larger than that observed experimentally by approximately a factor of three. While the simulated and experimental intensity modulations exhibited a satisfactory mutual resemblance, it was found that the relationship between the intensity modulations and the image mean intensity did not fit between simulation and experiment. As a consequence, it became standard procedure to disregard the image mean intensity when performing quantitative image comparisons and to compare only intensity modulations in a relative manner, involving a free scaling factor. The problem can be expressed more precisely in the following way. In HRTEM, it is common practice to multiply the image intensity by a normalization factor such that the mean intensity of the image adopts a dimensionless value of 1. After having normalized the experimental and simulated images to the same mean intensity of 1, the standard deviation (root-mean-square value, rms) of the intensity distribution reflects the image contrast. Due to the Stobbs factor problem, a discrepancy was frequently found in the contrast between simulation and experiment by approximately

a factor of 3. Image comparisons could then only be made in a relative manner by compensating for this discrepancy numerically without having a satisfactory explanation for it.

Recently, it has been reported that the neglect or underestimation of the modulation-transfer properties of the microscope's CCD camera in the course of image simulations is responsible for the largest part of the contrast discrepancy² and that, by incorporation of the measured camera modulation-transfer function (MTF), it is possible to achieve a quantitative fit of simulations to experimental images on an absolute contrast level³. A remaining minor residual mismatch can then be adjusted phenomenologically by lowering the simulated image contrast, which is still slightly too high, by convolution of the simulated image with a Gaussian function. We use the term effective image spread for the root-mean-square (rms) width of this phenomenologically applied Gaussian convolution function, which is applied to the simulated image in the present paper in addition to the camera MTF³.

An effective image spread value of $s = 16$ pm was required in the present work in order to obtain a perfect absolute intensity match between simulation and experiment. This value is consistent with the previously determined value of $s = 20$ pm for the same microscope type but a different material³. Image spread values on the order of 15 to 25 pm were explained recently by the presence of thermal magnetic field noise (Johnson noise) in the optical beam path of electron microscopes⁴.

Determination of the absorption constant

Since it is not standard procedure to work with the absolute image intensity, special emphasis is placed here on the modelling of absorption. Absorption accounts for electrons which have not been registered by the detector after interacting with the specimen, which can be due to a multitude of reasons such as blocking by an aperture, electron back-scattering or large delocalisation for high scattering angles. When compared to the vacuum level, a respective reduction of the mean image intensity can be measured for the region of interest, as shown in Supplementary Fig. 1. This experimentally observed intensity loss is incorporated into the image simulations on a phenomenological basis by the introduction of an imaginary part in the atomic scattering potential adopting the approach of Hashimoto, Howie and Whelan⁵. By using detailed diffraction simulations, it was found that the experimentally observed intensity drop-off of 1.3% at the determined object thickness of about 2.5 nm can be well reproduced in the simulations by using an absorption factor of 0.025, meaning that the absorptive imaginary part of the atomic scattering potential is set to 2.5% of the real part.

Details of column contrast

A single high-resolution TEM image is often interpreted as a projection of the atomic structure along the incident beam direction. Consequently, it has been shown in numerous publications that atomic column (x, y) coordinates in the detection plane can be deduced with nearly picometer precision from the positions of intensity peaks⁶. It has not, however, been evident whether a high-resolution image also provides sufficient information for the extraction of 3D atomic structure data. The question of whether and to what extent information about the atomic z -positions in the direction parallel to the incident electron beam can be determined is largely unexplored and has not been investigated quantitatively for the case of a 3D crystal. In the following paragraphs, an answer to this question is provided for the specific case of a single HRTEM image of an MgO crystal acquired along the [001] crystallographic zone axis.

We refer here to an HRTEM image of MgO [001], as shown in Fig. 1 in the main text, which was acquired under NCSI conditions. At the chosen imaging conditions, the (x, y) positions of the projected atomic columns can be identified by the (x, y) positions of the recorded intensity peaks. The two further properties that are required for 3D shape reconstruction are (i) the number of atoms in each atomic column and (ii) the z -position of each column. These two properties are in principle reflected by the heights and the shapes of the recorded intensity peaks. The decisive question is, whether unique column identification is possible by analysing the height and the shape of an intensity peak. This question can be split into two sub-questions: First, are the intensity changes that are produced either (i) by the addition/removal of 1 single atom, or (ii) by the minimal shift of a column by 1 atomic plane along the z -direction, large enough to be detected? Second, can the two different intensity changes (i) and (ii) be discerned from one another?

The fact that both questions can be answered positively even in the presence of image noise is demonstrated by the intensity difference signal shown in Supplementary Fig. 5 below. As examples, we consider here even-numbered columns of 8 atoms and odd-numbered columns of 9 atoms, which represent the majority of the column configurations in the investigated area. The crystal structure of MgO consists of two column types (A) and (B) with complementary Mg and O site occupations (checkerboard occupation). For any of the four possible reference column configurations (R) that can be formed by a combination of the properties even or odd occupation, and A or B type, all structural changes can be described by four elementary operations: an upward shift (U) of the column by one atomic plane, a downward shift (D) of the column by one atomic plane, the addition of one atom at the top surface (T) and the addition of one atom at the bottom surface (B). In total, 16

different minimal configuration change scenarios are therefore possible, as shown in Supplementary Fig. 5.

Strong intensity changes from 0.04 to 0.07 with respect to the mean value 1 occur due to an increase in the total column scattering power when adding one atom to a column. Comparatively smaller intensity changes between -0.022 and 0.022 occur due to a modified propagation distance after the last scattering event when changing the column z -position. Column z -shifts can only be realized by removing one atom from one surface and adding one atom to the opposite surface, in accordance with the surrounding MgO crystal structure. For cases of columns with an odd number of atoms, such elementary z -shifts are always accompanied by small additional changes in the total scattering power, since an Mg atom is exchanged by an O atom, or vice versa. The diagrams in Supplementary Fig. 5 show that all possible minimal peak intensity changes with respect to the respective reference columns, and in particular also the comparatively small z -shift induced changes, are larger than the peak intensity measurement error imposed by noise. Second, the peak intensity changes caused by the four elementary configurational changes differ from one another by more than the estimated peak intensity measurement error, which guarantees not only detectability but also distinguishability. As a consequence, the five minimally differing configurations (R, U, D, T and B) can be distinguished and identified in the presence of realistic image noise. The root-mean-square error for measuring peak intensities from the experimental image amounts to 0.003, which has been carefully determined by means of statistical error propagation when fitting a Gaussian peak function to representative intensity peaks within a circular area of 60 pm radius.

It is important to note that the intensity differences shown in Supplementary Fig. 5 have not been calculated for isolated atomic columns, but for columns that are packed into a consistent environment of columns with identical heights to that of the reference column. The intensity differences are moreover not fixed numbers, but depend on various experimental factors, such as the object tilt and the chosen mean defocus value. More importantly, the principal demonstration of signal uniqueness, as shown in Supplementary Fig. 5, was made for educational purposes on the basis of peak intensity levels alone. In our actual work we used root-mean-square intensity minimization on a sub-pixel level for the comparison of simulation and experiment, which includes the peak shapes in two dimensions and thereby increases the detection sensitivity significantly over that of a pure peak height comparison. The robustness of the latter column identification approach against image noise is investigated statistically by means of a Monte Carlo simulation test in the following section.

Statistical confidence analysis

3D reconstruction is based here on finding the simulated image that provides a best fit to the experimental input image on an absolute intensity scale. The root-mean-square (rms) difference between the experimental and simulated image within a small image area is used as an indirect measure of the agreement between a model structure and the real crystal structure of the investigated sample. The best-fitting model is identified by a minimum rms difference when varying the microscope and object parameters in the image simulations. In this approach, the atomic z -positions represent only a small sub-space of the complete multi-dimensional parameter space in the search for the minimum difference. However, several assumptions apply in the present case, which allow the problem to be investigated in a parameter space of greatly reduced dimensions:

- (i) Each atomic column is a discrete string of periodically alternating Mg and O atoms, which is assumed to be free of vacant sites and impurities.
- (ii) The MgO crystal is compact and its thickness is limited to a few nanometres within the investigated volume.
- (iii) Globally valid parameters, such as optical aberrations and the exact object orientation, can be determined beforehand and considered to be sufficiently well known (see Supplementary Table 1).
- (iv) The lateral (x, y) coordinates of the atomic columns can be determined independently of their vertical z -positions.
- (v) The NCSI imaging mode provides such small contrast delocalization that the image intensity at each column of interest is only negligibly influenced by that of the neighbouring atomic columns.

The instrumental imaging properties referred to in assumption (iii), such as the instrumental resolution and camera characteristics, can be measured using independent methods. Other global imaging parameters in assumption (iii), such as the defocus, 2-fold astigmatism and object tilt, depend on the particular experiment and can be refined in advance by using a separate reference image area that has no overlap with the image region of interest for the 3D reconstruction.

Assumptions (iv) and (v) allow the atomic z -coordinates within each atomic column to be determined independently of the (x, y) column coordinates and also independently of the atomic configurations of neighbouring columns. The independent treatment of individual atomic columns allows the dimensions of the search space to be reduced to that of $d = n$ unknowns, corresponding to the z -coordinates of the n atoms residing in a single column.

It is important to note that assumptions (iii-v) discussed so far are only auxiliary assumptions, which are used below to facilitate Monte Carlo investigations using simulated images. In the experimental case, which is treated in the main text, these assumptions were not made because the refinement of global parameters, the refinement of the atomic positions and the refinement of the site occupancies was performed repeatedly in a global optimization cycle, taking into account the possibility of extremely weak cross-dependencies between these principal parameter classes.

By applying the primary assumption (i), the search space becomes only 2-dimensional ($d = 2$), since the coordinates of the n atoms within a column can be determined solely with reference to the position z_{top} terminating the atomic column at the top, and the position z_{bot} terminating the column at the bottom (see the schematic drawings in Supplementary Fig. 6 and Supplementary Fig. 8). The general case of a 3D volume reconstruction is reduced by assumption (i) to the special case of a 3D surface morphology reconstruction.

Finally, assumption (ii) restricts the column heights to a few nanometres and thereby limits the range of possible values for z_{bot} and z_{top} . In the present investigation, the range of possible z -positions is restricted to 20 atomic layers, which corresponds to a crystal thickness of approximately 4 nm.

In a first preparatory step, high-resolution TEM images were calculated for each possible column configuration in the limited search space $\{z_{\text{bot}}, z_{\text{top}}\}$, taking into account the parameters listed in Supplementary Table 1 and using the measured detector MTF^{2,3}. The images were simulated at the same spatial sampling rate as in the experiment. Representative substitutes for real experimental images, in which the underlying atomic configuration is known exactly, were subsequently constructed from these simulated images by adding simulated noise. The resulting noisy images are referred to as pseudo-experimental images below and were used as input for the subsequent steps in the procedure. Noise was synthesized according to a Poisson distribution based on the average number of electrons collected per pixel. The resulting noise distribution was subsequently convoluted by the noise transfer function of the experimental detector⁷ and finally added to the simulated images. By following this procedure, the noise amplitude in the vacuum region in the experimental image of Fig. 2a of the main text is reproduced in a pseudo-experimental image without atoms when using the same mean image intensity.

For each relevant atomic column configuration ($z_{\text{bot}}, z_{\text{top}}$), we calculated several hundred pseudo-experimental input images with mutually different noise contents. Each of these pseudo-experimental input images was compared to all of the relevant noise-free simulated images that can occur in the search space of the allowed atomic column configurations. A figure-of-merit was established by calculating the rms difference between the pseudo-

experimental and simulated intensity distributions in a small circular region of interest (ROI) with a radius of 7 pixels, where the pixel distance is 0.0104 nm. The ROI is centred on the position of the intensity peaks in the two images independently. The best-fitting configuration $(\zeta_{\text{bot}}, \zeta_{\text{top}})$ yielding the minimum rms difference is registered in normalized counting statistics. By using hundreds of pseudo-experimental images as input, approximate probability distributions $p(z_{\text{bot}}, z_{\text{top}}, \zeta_{\text{bot}}, \zeta_{\text{top}})$ were finally obtained for each column configuration $(z_{\text{bot}}, z_{\text{top}})$. The value p approximately reflects the likelihood of identifying the existing atomic column configuration $(z_{\text{bot}}, z_{\text{top}})$ underlying an experimental image by a certain best-fitting model configuration $(\zeta_{\text{bot}}, \zeta_{\text{top}})$. In the case of correct identification it is required that $(\zeta_{\text{bot}}, \zeta_{\text{top}}) = (z_{\text{bot}}, z_{\text{top}})$, and the corresponding value $p(z_{\text{bot}}, z_{\text{top}}, z_{\text{bot}}, z_{\text{top}})$ reflects the success rate of the applied best-fit strategy assuming that further systematic errors are absent. The success rate depends on the column configuration $(z_{\text{bot}}, z_{\text{top}})$ and on the amount of noise present in the experiment.

The resulting probability distributions extend predominantly along the main diagonal and are very narrow along the perpendicular direction. Selected example distributions are displayed in Supplementary Fig. 7 in form of two-dimensional plots of the configuration space $\{z_{\text{bot}}, z_{\text{top}}\}$, where the underlying input configuration $(z_{\text{bot}}, z_{\text{top}})$ is located at the centre of the plot. In these plots, changes $\Delta z_{\text{bot}} = (\zeta_{\text{bot}} - z_{\text{bot}})$ of the bottom termination are registered at different positions along the horizontal axis, while changes $\Delta z_{\text{top}} = (\zeta_{\text{top}} - z_{\text{top}})$ of the top termination are registered at different positions along the vertical axis. Steps on the main diagonal therefore correspond to configuration changes involving the removal of an atom from one surface and adding an atom to the other surface at the same time, thereby realising shifts along z . The extended distributions along this direction therefore indicate the uncertainty in identifying the correct z -position. The column z -position changes by one atomic plane every two pixels along the main diagonal, since the distribution plots in Supplementary Fig. 7 sample configuration changes in steps of half atom occupancies at the surface sites. Despite the spread along the main diagonal, the majority of the distribution is located at the correct atomic plane for columns that contain 5 or more atoms. The very narrow distribution along the perpendicular diagonal direction indicates that the correct number of atoms is safely identified in all cases with even half atom precision. The vast majority of the distributions exhibit only one pronounced sufficiently narrow maximum at the correct position, which indicates that the chosen strategy for identifying atomic columns by finding the best-fitting simulation is correct within the investigated search range.

A comprehensive overview of the reliability of 3D shape determination from a single HRTEM image is presented in Supplementary Fig. 8. The graphs show, for all possible column configurations $(z_{\text{bot}}, z_{\text{top}})$ in the investigated search space, the success rates P_n and P_z , where P_n is the success rate for correctly determining the number n of column atoms,

and P_z is the success rate for correctly determining the position z of an atomic column. Both success rates P are calculated on the basis of the probability distributions $p(z_{\text{bot}}, z_{\text{top}}, \zeta_{\text{bot}}, \zeta_{\text{top}})$. The values of $P_n(z_{\text{bot}}, z_{\text{top}})$ are determined by adding the values of p for all configurations $(\zeta_{\text{bot}}, \zeta_{\text{top}})$ that have the same number of atoms as in the input configuration $(z_{\text{bot}}, z_{\text{top}})$. The values of $P_z(z_{\text{bot}}, z_{\text{top}})$ are calculated by adding the values of p for all configurations $(\zeta_{\text{bot}}, \zeta_{\text{top}})$, where the bottom atom is located in the same atomic plane as in the input configuration $(z_{\text{bot}}, z_{\text{top}})$, regardless of its partial occupation level.

The graphs in Supplementary Fig. 8 span the same two-dimensional configuration space as that in the distribution plots of Supplementary Fig. 7, with the bottom termination z_{bot} varying along the horizontal axis and the top termination z_{top} varying along the vertical axis. Different “bin sizes” or “sensitivities” have been used for identifying atomic column configurations: While only columns that have a discrete integer number n of atoms per column are considered in Supplementary Figs. 8a and 8b, Supplementary Figs. 8c and 8d also consider columns that have half atom occupations at the two terminating atomic positions. Partial occupations of surface atom positions may, for example, occur when single atoms change their position during image exposure by moving over the specimen surface. White pixels represent configurations for which $z_{\text{bot}} \geq z_{\text{top}}$, *i.e.*, where no atoms are present. The colour scale denotes the fraction P of correct identifications within the statistical set. Consequently, the missing fraction $1 - P$ denotes the sum of false identifications that may be distributed over several neighbouring configurations.

The results of the calculations indicate that the number n of atoms in a column can be determined in general with very high confidence, even allowing for half-atom sensitivity. In the graphs shown in Supplementary Fig. 8, the success rate P_n decreases slightly with increasing n . This slight reduction in atom counting reliability occurs when the column length approaches half of the extinction length, which corresponds to a half period of the Pendelloesung dependence in dynamical diffraction theory. The determination of the column z -position is also reliable with high confidence for columns that contain 5 or more atoms. For very short columns that consist of one to four atoms, the success rate P_z drops below 50%, which indicates inaccurate determination of the z -position in such cases. However, only 2 out of 70 atomic columns fall into this category in the entire reconstructed crystal volume. The vast majority of the atomic columns contain between 7 and 10 atoms, which allows one to determine their z -positions with a high degree of confidence.

A reduced subset of the general success rates P_n and P_z , which corresponds (for reasons of convenience) only to the atomic column configurations found in this work, is shown in Supplementary Fig. 9. The position of each coloured square in graphs (b) and (c) refers to a specific atomic column configuration that was previously determined at the same relative position in the experimental image (a). For this subset of atomic column configurations, the

success rates P_n to determine the number of atoms n with half atom precision are between 78% and 95%, whereas the z -positions of such columns can be determined with success rates P_z of between 55% and 88%, except for the two columns at the sample edge, which contain only one or two atoms. It is important to note that the z -error of the minority fraction $1 - P_z$, where mis-identification of the column z -position could have occurred, is in general only ± 1 lattice plane.

***Ab initio* calculations**

Ab initio calculations were performed to investigate possible site preferences for the adsorption of C atoms on an (001) MgO surface. A supercell containing 4 MgO layers along the z -axis (16 atoms) was used to model the thin MgO crystal. The present results were obtained by using the ABINIT code⁸ and the Perdew-Burke-Ernzerhof (PBE) generalized gradient approximation (GGA)⁹. The calculations were based on a plane-wave basis truncated at 40 hartree and were performed on a $4 \times 4 \times 2$ k -point mesh within the first Brillouin zone.

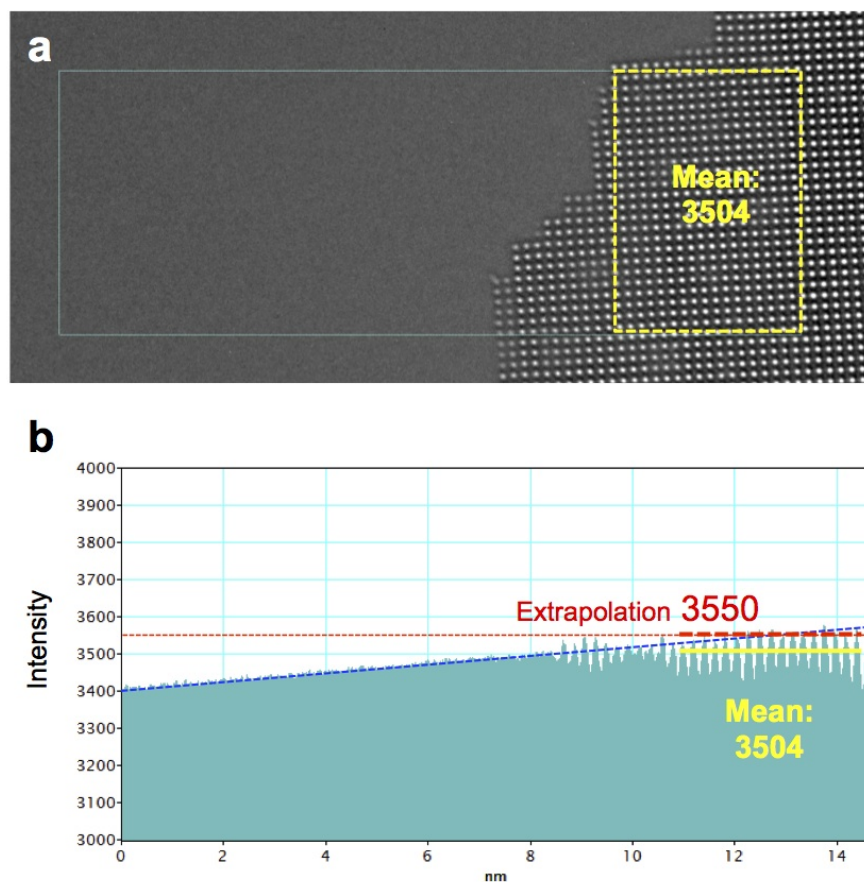
The MgO slab was first relaxed in order to obtain its stable equilibrium structure. Subsequently, a C atom was added to the top surface of the MgO slab at four selected positions: i) the centre of an Mg-O edge, ii) the centre of an Mg-O square, iii) above an Mg atom and iv) above an O atom, as shown in Supplementary Fig. 9. In a first test, the C atom was shifted slightly away from the initial positions defined according to i) – iv), and the system was then *allowed* to relax again. In all instances, this relaxation process resulted in a movement of the C atom towards a neighbouring O atom. To further test whether it is indeed energetically favourable for the C atom to remain above an O atom, we fixed all of the atoms in the MgO slab and allowed only the C atom to relax along the z -axis. The energy of the resulting four configurations is shown in Supplementary Table 2, which highlights the fact that the C atom is most likely to stay on top of an O atom since that is where it can adopt the lowest energy configuration. The alternative scenario, where the C atom resides above an Mg atom, yields the highest energy, presumably because C and Mg atoms cannot form a chemical bond. The other two cases (C_{iii} and C_{iv}) have medium energies, since both O and Mg atoms affect the C atom at these two positions.

Supplementary Table 1. Specimen and electron-optical parameters corresponding to the image shown in Fig. 2. Except for the Debye-Waller factors (DWFs), all values were globally refined using an iterative procedure. The reference direction for the azimuth angles is the detector *x*-axis. The parameters *B* used to calculate the Debye-Waller factors of Mg and O were taken from Ref. 10.

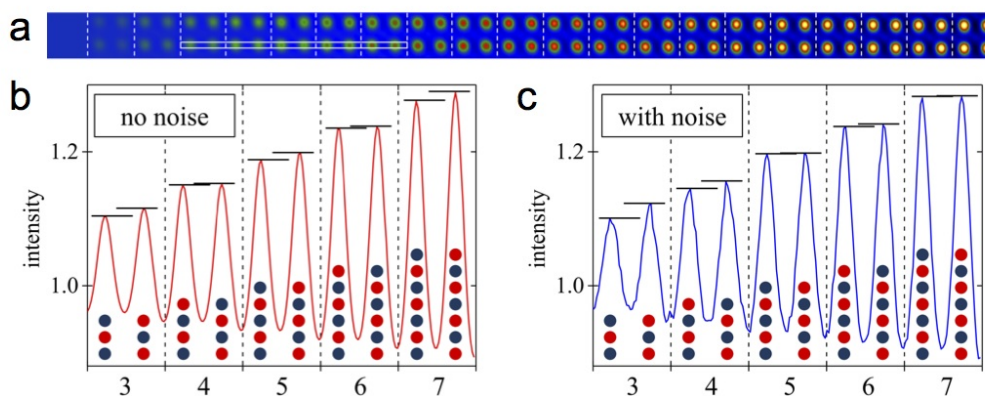
Parameter	Magnitude	Azimuth/deg
Specimen thickness	0.2 – 2.5 nm	
Specimen tilt	15.0 mrad	0
Absorption	0.025	
Defocus	5.1 nm	
2-fold astigmatism	1.0 nm	130
3-fold astigmatism	30 nm	0
Coma	40 nm	10
Spherical aberration	–15 μm	
Defocus spread (rms)	2.9 nm	
Image spread (rms)	0.016 nm	
DWF, B_{Mg}	0.0030 nm ²	
DWF, B_{O}	0.0034 nm ²	

Supplementary Table 2. Energies of C atoms adsorbed on different geometrical positions (i-iv) of the MgO surface, as indicated in Supplementary Fig. 9. The energies were obtained using ab initio calculations and are given relative to the C-adsorbed-on-O case.

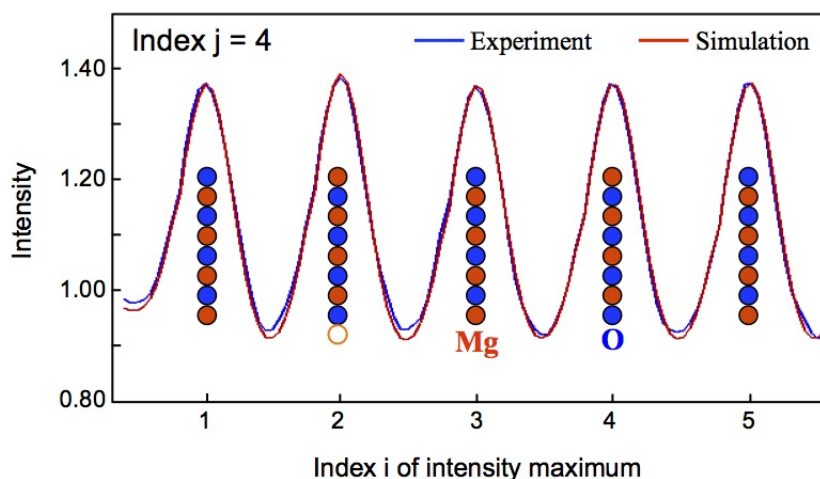
Position above	Energy (eV)
O atom (C_i)	0
Mg atom (C_{ii})	1.814
Center of Mg-O edge (C_{iii})	0.939
Center of Mg-O square (C_{iv})	0.185



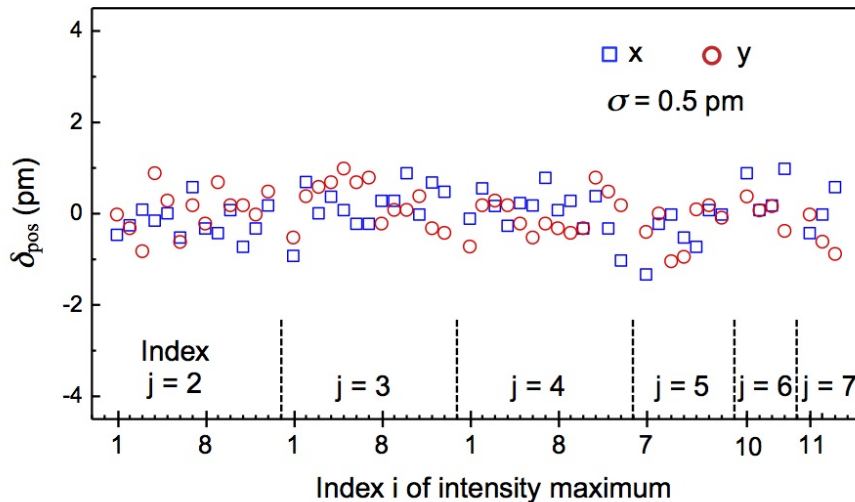
Supplementary Fig. 1 | Determination of the phenomenological electron absorption parameter for MgO. (a) HRTEM image including vacuum (left) and specimen area (right). (b) Intensity profile obtained by scanning the image intensity from left to right within the large blue frame shown in (a). The vacuum intensity, which increases towards the specimen due to slightly uneven electron illumination, is extrapolated into the specimen area (yellow frame). The intensity resulting from the vacuum extrapolation is 3550, whereas the mean value measured in the yellow framed area is 3504 counts. The resulting count-rate ratio is thus $3504/3550 \approx 0.987$, which means that 1.3% of the electrons traversing the indicated crystalline area are not registered in the image.



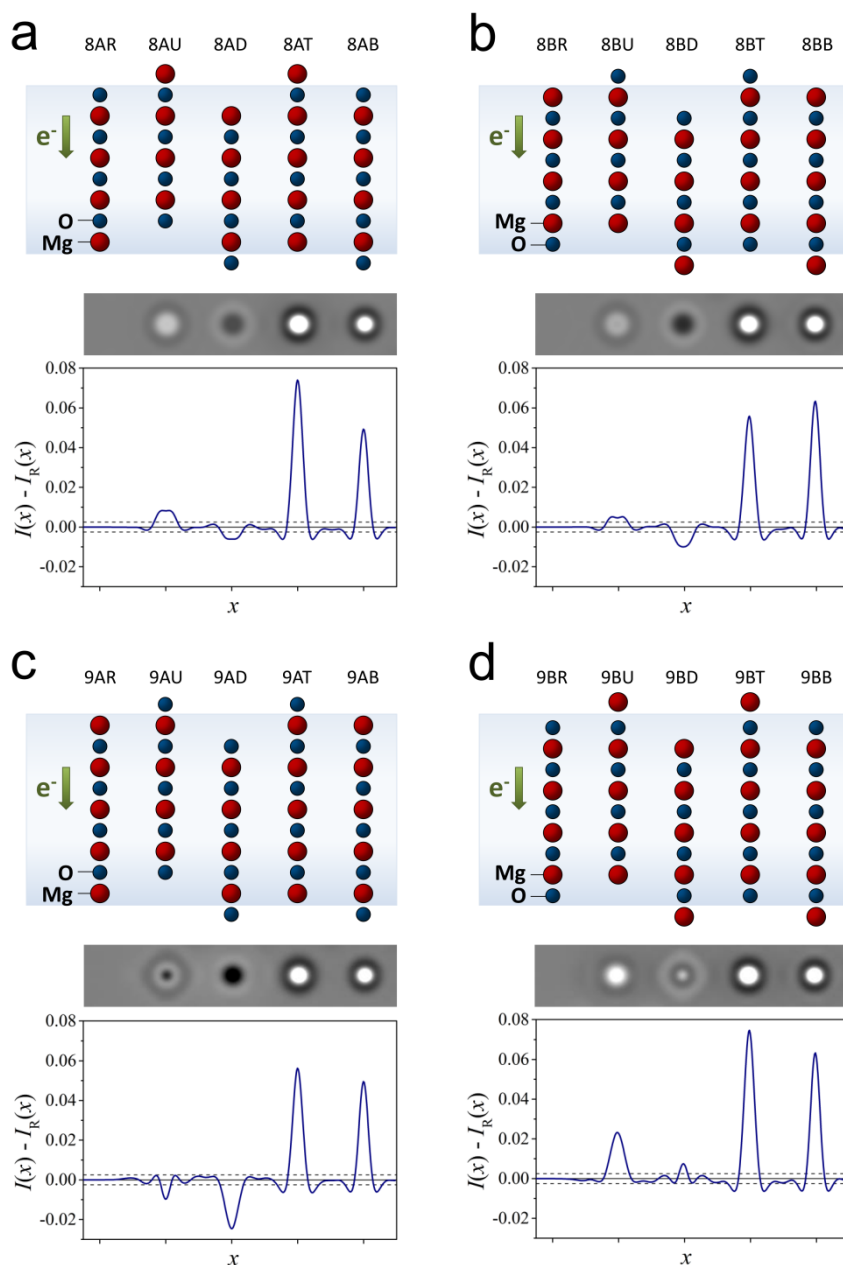
Supplementary Fig. 2 | Intensity changes upon inversion of the occupation sequence. (a) Sequence of 21 images simulated for increasing object thickness between zero atomic layers (left) and 20 atomic layers (right). The image size of 0.42 nm × 0.42 nm corresponds to the area of an MgO unit cell projected along the [001] direction. The line scans of the image intensity are extracted from the rectangular area marked in (a), assuming noise-free conditions (b), and additional Poisson noise (c) due to the finite number of detected electrons. The standard deviation of the simulated Poisson noise is equal to that in the experimental image shown in Fig. 2a. Mg atoms are depicted by red dots and O atoms by blue dots. Horizontal black lines indicate the peak intensities at the atomic column positions. Under noise-free conditions, columns containing an odd number of atoms exhibit a clear intensity difference upon inversion of occupation, while columns containing an even number of atoms exhibit a much smaller intensity difference. The intensity difference associated with a single odd-numbered column may be hidden in certain cases by noise. However, the correct occupation variant can be determined safely by using *a-priori* knowledge of the checkerboard sequence of atom types and by combining the signal of all odd-numbered columns in the image.



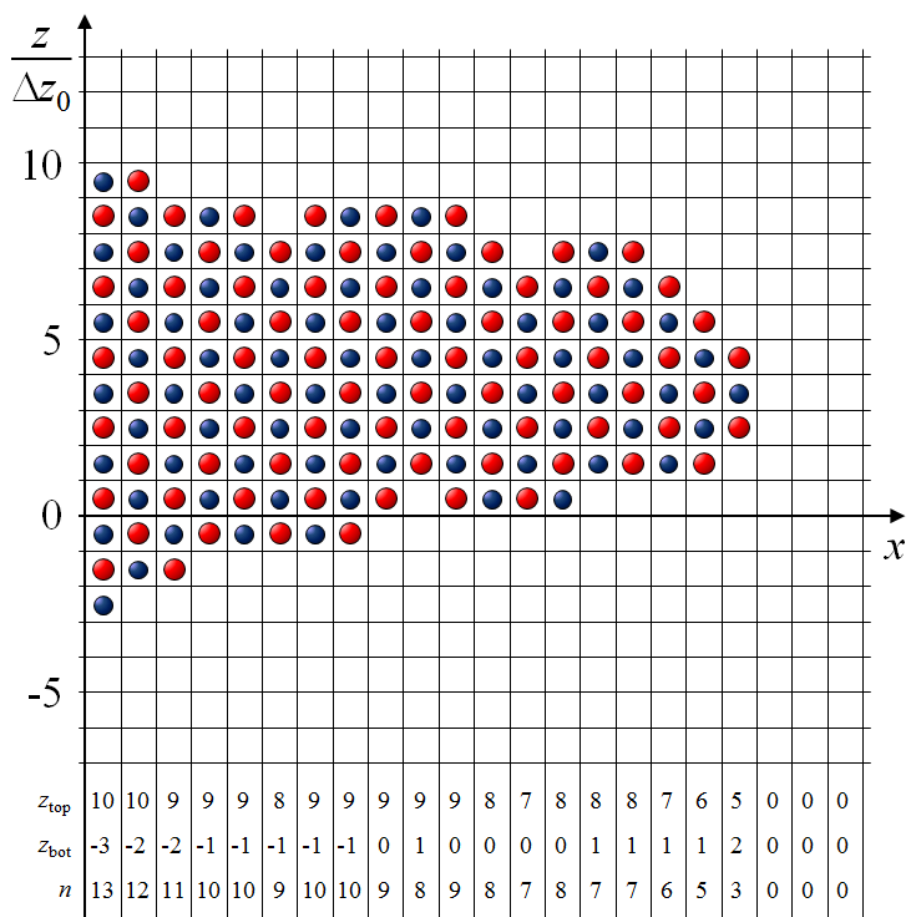
Supplementary Fig. 3 | Comparison of simulated and experimental intensity profiles on an absolute contrast scale. The indices i and j identify individual atomic columns according to the scheme defined in Fig. 2a. The open circle denotes 50% occupancy at a surface site.



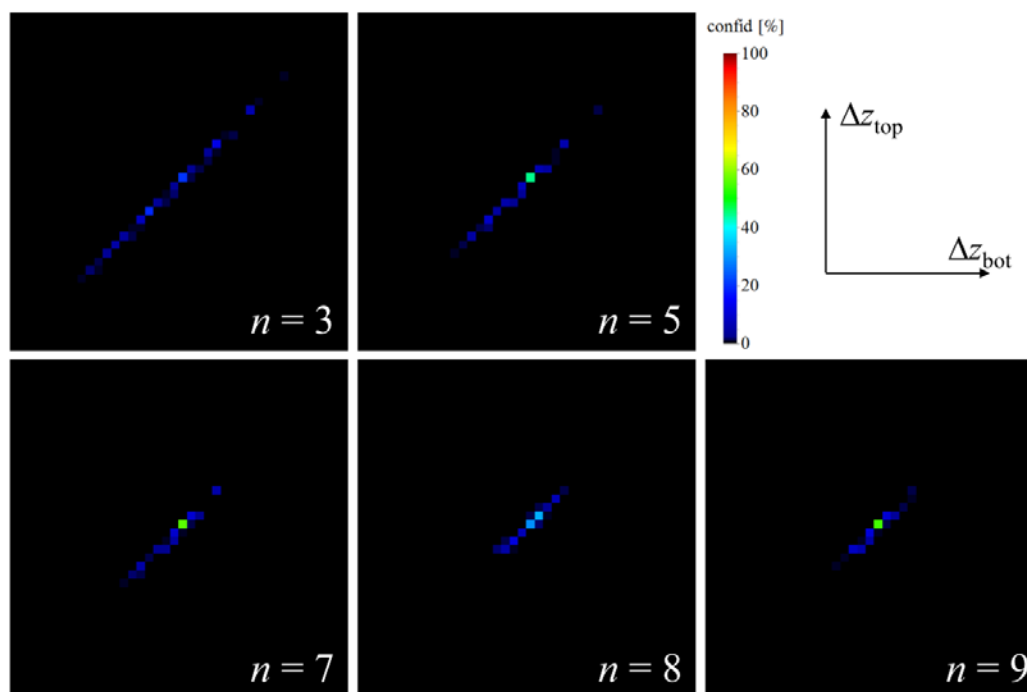
Supplementary Fig. 4 | Position deviations δ_{pos} in the intensity maxima between experiment and simulation for the x (squares) and y (circles) directions. The root-mean-square position deviation σ is 0.5 pm in both the x and the y direction. The indices i and j identify individual atomic columns according to the scheme defined in Fig. 2a.



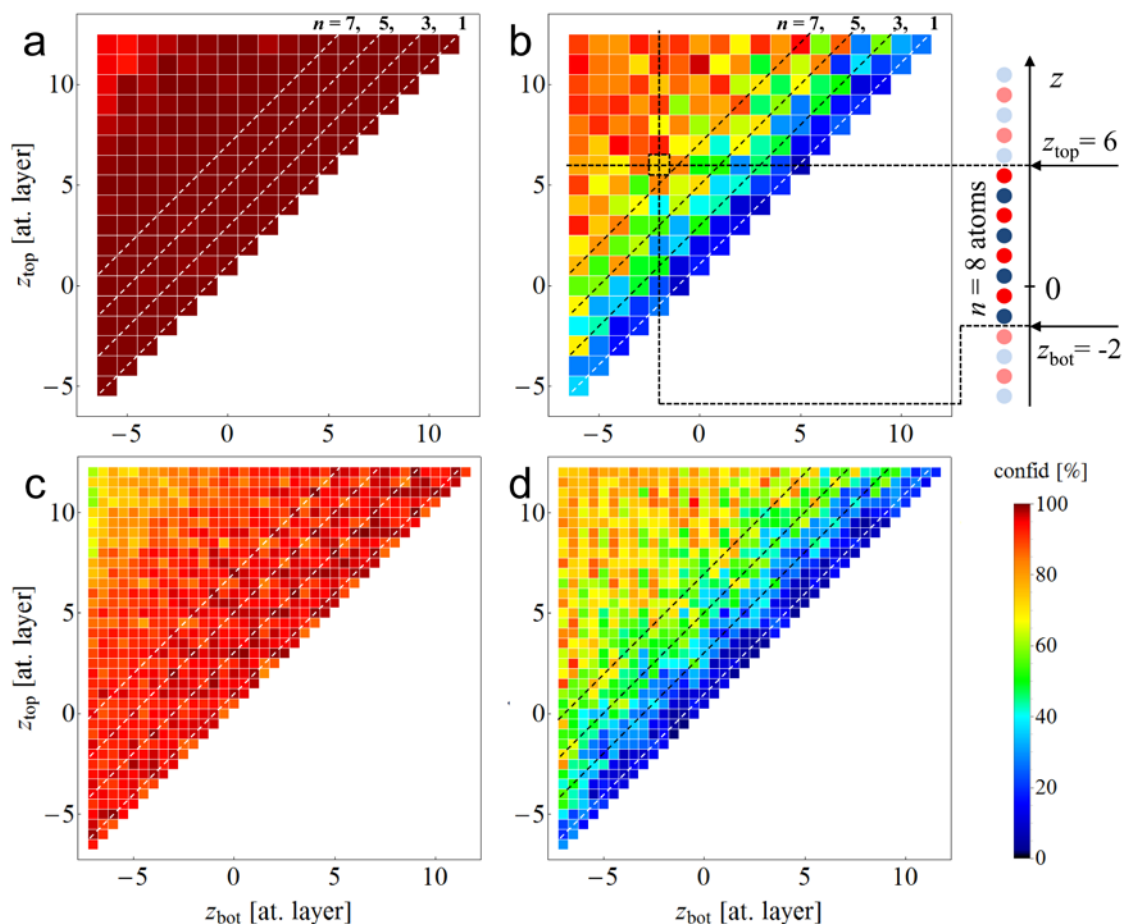
Supplementary Fig. 5 | Illustration of minimal changes in atom number and z -position applied to reference columns containing either an even number of 8 atoms (a, b) or an odd number of 9 atoms (c, d). Four different reference columns (R) must be considered, since two occupation variants (A) and (B) with complementary site occupations exist for each of the even and odd-numbered atomic columns. Minimal configuration changes with respect to the reference columns (R) are an upward shift (U) or a downward shift (D) of the column by one atomic plane along the z -axis, as well as adding one atom at the top surface (T) or at the bottom surface (B). z -shifts are realized by removing one atom from one surface and adding one atom at the opposite surface in accordance with the surrounding MgO crystal structure. The image stripes and line scans below the atomic configurations show the calculated intensity differences with respect to the reference columns in two dimensions, and in a one dimensional line scan representation, respectively. The dashed horizontal lines in the line scan diagrams denote the estimated error for extracting peak intensity values from the experimental HRTEM image. The displayed intensity values were calculated for the ideal case of untilted columns and are scaled with respect to a vacuum intensity of 1.



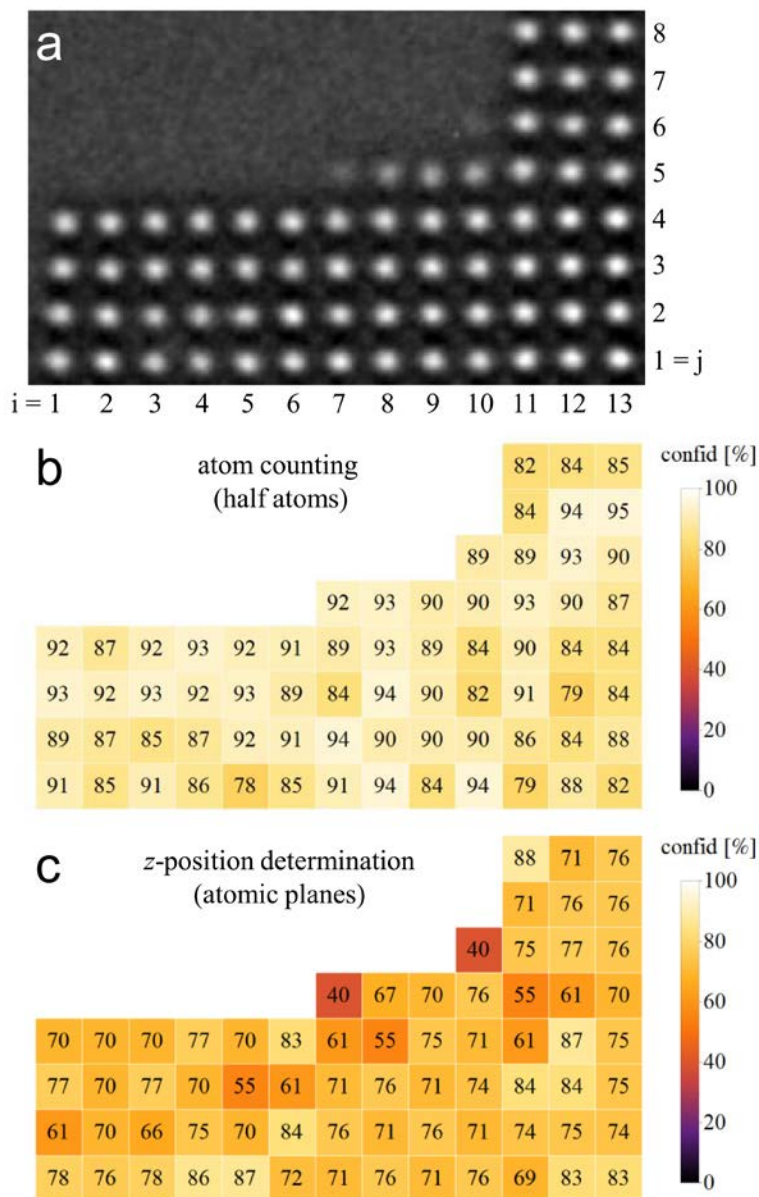
Supplementary Fig. 6 | Illustration of the notation scheme used for defining atomic column configurations. The scheme uses the z -coordinates z_{bot} and z_{top} belonging to the bottom and top atoms of an atomic column. Examples are given for the (010) plane of a compact MgO crystal, with Mg atoms indicated by red spheres and O atoms indicated by blue spheres. The values z_{bot} and z_{top} reflect the z -positions of the bottom and top atoms in units of the interatomic distance $\Delta z_0 = 0.2107$ nm. The number $n = (z_{\text{top}} - z_{\text{bot}})$ is the number of atoms in a column.



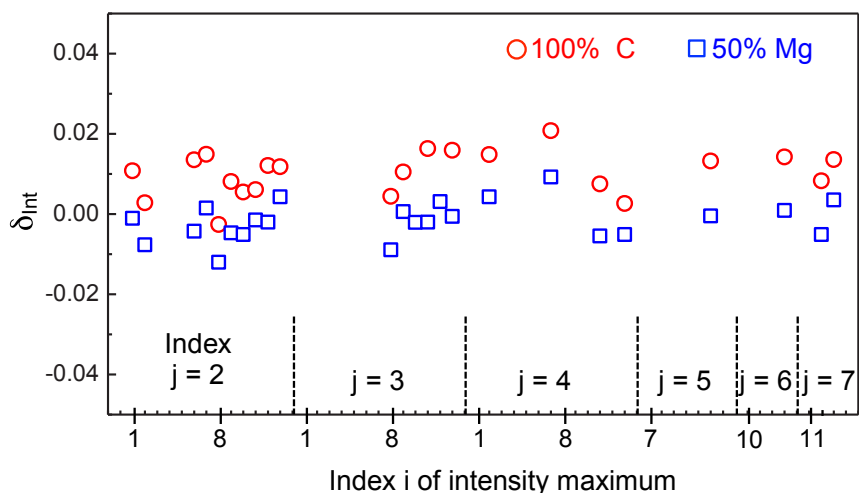
Supplementary Fig. 7 | Result of column identification attempts obtained by finding the simulated image that provides a best fit to an experimental image. Reference column configurations ($z_{\text{bot}}, z_{\text{top}}$) at the centres of the plots were chosen in order to generate a multitude of pseudo-experimental input images that differ from each other only by the added noise. Subsequently, it was attempted to identify each of these pseudo-experimental input images by finding the best-fitting simulated image based on column configurations ($\zeta_{\text{bot}}, \zeta_{\text{top}}$). The five plots differ in the number of atoms n belonging to the input column configuration ($z_{\text{bot}}, z_{\text{top}}$). In the case of a 100% successful recognition rate, the result of the output distribution would be a perfect delta function located at the centre ($z_{\text{bot}}, z_{\text{top}}$) of the plot. As a result of the addition of experimental noise, off-centre configurations ($\zeta_{\text{bot}}, \zeta_{\text{top}}$) are incorrectly found, forming a distribution around the correct centre location. The displayed pixel size amounts to only a half occupation in the top and bottom atomic layers. The arrow length at the top right corresponds to a configuration change $(\Delta z_{\text{bot}}, \Delta z_{\text{top}}) = (\zeta_{\text{bot}} - z_{\text{bot}}, \zeta_{\text{top}} - z_{\text{top}})$ of 10 atomic layers. The distributions are normalized in such a way that summation over all pixel values, indicated here in false colour, results in a probability of 1. The linear diagonal shape of the distributions indicates a defocus (or z -position) uncertainty that becomes rapidly smaller as the number of atoms n in a column increases. The narrow extent of all of the distributions in the perpendicular diagonal direction indicates that the number of atoms in a column can be identified reliably in all instances.



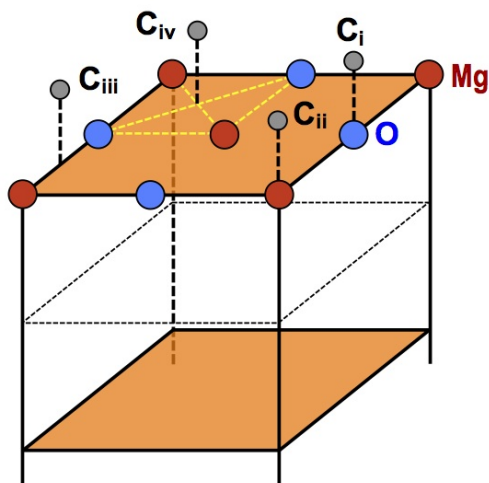
Supplementary Fig. 8 | Success rates P_n for the correct identification of the atom number n (a, c), and P_z for the correct identification of the column z -position (b, d) from a single HRTEM image of MgO [001]. One pixel in the graphs corresponds to an atomic column configuration that is defined by the two variables z_{top} and z_{bot} . These variables are the z -positions terminating the column above the top atom and below the bottom atom, as illustrated in (b). Column configurations with $n = 1, 3, 5$ and 7 atoms are marked by dashed diagonal lines. Moving along such diagonal lines corresponds to a rigid shift of columns with a constant number of atoms $n = z_{\text{top}} - z_{\text{bot}}$ with respect to a common reference plane $z = 0$. The false colour denotes the success rates obtained. The success rates were determined by Monte Carlo simulations on the basis of the experimentally observed rms noise variation of $\sigma_n = 0.013$ using the global imaging parameters of Supplementary Table 1. The success rates displayed refer to a target precision of single atoms (a, b), and half atoms (c, d) in the occupation of the respective surface sites. Since the target precision becomes more demanding for half occupations at the surface, the corresponding success rates drop accordingly in (c, d).



Supplementary Fig. 9 | Confidence levels for the atomic column configurations identified in the experimental image. The images below the experimental image (a) denote the confidences P_n for counting correctly the number of atoms in each column with half atom precision (b), and P_z for determining correctly the column z -position with atomic plane precision (c). The indicated confidence values are a subset of the confidence values shown in Supplementary Figs. 8c and 8d.



Supplementary Fig. 10 | Intensity difference δ_{int} between experiment and simulation at Mg peak positions. The blue squares refer to a simulation model that allows for half-occupied Mg sites at the surface (see Fig. 4). The red circles refer to a simulation model that incorporates full C-atom occupation instead of a half Mg-atom occupation. Both models perform equally well, since the magnitude of the residual fitting differences δ_{int} does not differ significantly between the two scenarios.



Supplementary Fig. 11 | Positions i-iv considered in the *ab initio* calculations described in the text for analyzing the adsorption of C atoms on an MgO (001) surface.

References

1. Hýtch, M. J. & Stobbs, W. M. Quantitative comparison of high resolution TEM images with image simulation. *Ultramicroscopy* **53**, 191-203 (1994).
2. Thust, A. High-resolution transmission electron microscopy on an absolute contrast scale. *Phys. Rev. Lett.* **102**, 220801 (2009).
3. Jia, C. L. *et al.* Atomic-Scale Measurement of Structure and Chemistry of a Single-Unit-Cell Layer of LaAlO₃ Embedded in SrTiO₃. *Microsc. Microanal.* **19**, 310-318 (2013).
4. Uhlemann, S., Müller, H., Hartel, P., Zach, J. & Haider, M. Thermal Magnetic Field Noise Limits Resolution in Transmission Electron Microscopy. *Phys. Rev. Lett.* **111**, 046101 (2013).
5. Hashimoto H., Howie A. & Whelan M. J. Anomalous Electron Absorption Effects in Metal Foils: Theory and Comparison with Experiment. *Proc. R. Soc. Lond. A* **21**, 80-103 (1962).
6. Houben, L., Thust, A. & Urban, K. Atomic-precision determination of the reconstruction of a 90° tilt boundary in YBa₂Cu₃O_{7- δ} by aberration corrected HRTEM. *Ultramicroscopy* **106**, 200-214 (2006).
7. Meyer, R. R. & Kirkland, A. The effects of electron and photon scattering on signal and noise transfer properties of scintillators in CCD cameras used for electron detection. *Ultramicroscopy* **75**, 23-33 (1998).
8. The ABINIT code is a common project of the Université Catholique de Louvain, Corning Incorporated, and other contributors (URL <http://www.abinit.org>).
9. Perdew, J. P., Burke, K. & Ernzerhof, M. Generalized Gradient Approximation Made Simple. *Phys. Rev. Lett.* **77**, 3865-3868 (1996).
10. Lawrence, J. L., Debye-Waller factors for magnesium oxide. *Acta Cryst. A* **29**, 94-95 (1973).